Orlicz risks for assessing stochastic streamflow environments: a static optimization approach

Hidekazu Yoshioka[1] · Haruka Tomobe[2] · Yumi Yoshioka[3]

Abstract

This study applies novel risk measures, called Orlicz risks, to the risk and uncertainty evaluation of the streamflow discharge as a primary driver of hydrological and hydraulic processes of interest in civil and environmental engineering. We consider the mixed moving average process governing the discharge whose statistics are explicitly represented as some product of a time-scale characterizing the flow attenuation and a jump moment governing the size and frequency of jumps. The classical Orlicz risks are extended so that not only the upper tail risk but also the lower one of the jump size and attenuation of the discharge can be evaluated within a single mathematical framework. Further, the risk and uncertainty can be individually quantified in a tractable manner by the proposed Orlicz risks. Computing the Orlicz risks reduces to solving a pair of novel static optimization problems that are solvable semi-analytically. The risk and uncertainty involved in the streamflow dynamics can be consistently evaluated by specifying few user-dependent parameters. The associated Radon–Nikodym derivatives as the worst-case model uncertainties are obtained as byproducts. Sufficient conditions for the well-posedness of the Orlicz risks are discussed and numerical algorithms for computing them are presented. We finally apply the proposed framework to a statistical analysis of the streamflow discharge time series data collected at mountainous river environments.

1 Introduction

1.1 Research background

1.1.1 Stochastic process models for streamflow discharge

Streamflow environments are dynamically changing in time due to stochastic forcings such as precipitation and runoff processes (Wing et al. 2020; Shabestanipour et al. 2023). The dynamic nature of streamflow environments is of critical importance from a variety of sustainability aspects, such as the transport of riverbed materials governing river morphology (Lague 2014) and chemics determining river water quality (Li et al. 2022), the life history of freshwater fish species (Archdeacon et al. 2022; Malone et al. 2022), the infrastructure investment for mitigating flood risks (Hamilton et al. 2022), the reservoir operation (Baker et al. 2022), and the hydropower generation (Ávila et al. 2021).

The streamflow discharge, which is the water volume that passes through a river cross-section in a unit time, is the primary variable governing streamflow environments. The dynamically changing stochastic nature of streamflow environments has been effectively captured by jump-driven stochastic process models (Botter et al. 2013). The common mathematical structure of such models is that a jump in a time series represents a flood event that attenuates in time, and key statistics such as moments, autocorrelation functions (ACFs), and further probability density of the discharge are available in closed forms. These models have been widely employed for the investigations of streamflow

✉ Hidekazu Yoshioka
yoshih@jaist.ac.jp

1 Japan Advanced Institute of Science and Technology, 1-1 Asahidai, Nomi, Ishikawa 923-1292, Japan

2 Tokyo Institute of Technology, 4259 Nagatsuta-cho, Midori Ward, Yokohama 226-0026, Japan

3 Shimane University, Nishikawatsu-cho 1060, Matsue 690-8504, Japan

environments by taking advantages of this remarkable property; such examples are the evaluation of hydrological river network connectivity (Garbin et al. 2019), the stochastic analysis of flow regulations due to human water use (Ferrazzi and Botter 2019), the simulation of particulate transport in streamflow environments (Catalàn et al. 2022), the river incision analysis under climate changes (Desormeaux et al. 2022), the macroscopic water balance analysis in the catchment scale (Daly et al. 2019), the drought risk evaluation (Li et al. 2023), and the streamflow regulation aiming at the environmentally-friendly as well as stable water supply (Yoshioka et al. 2023).

Since the stochastic process models are coarse-graining of physical processes that govern the streamflow dynamics, they inherently contain modelling errors in coefficients and parameter values. The flood attenuation was originally considered to be exponential, while the sub-exponential ones have been found to better fit to the real discharge data, effectively reflecting the watershed heterogeneity; the nonlinearization (Botter et al. 2009; Dralle et al. 2018; Li and Ameli et al. 2022) and model aggregation (Yoshioka 2022) have been discussed for resolving this issue although these approaches are still conceptual and are not fully physical. Properly modelling the flood attenuation is important for ecological assessment of riparian zones (Philipsen and Rood 2022) and the flood risk management (Asselman et al. 2022). In addition, modeling flood events with extremely large discharges is crucial for the hazard prediction (Guo et al. 2022; Merz et al. 2022), while the data to quantify such rare events is usually not abundant. Assessing stochastic process models under the model uncertainty is therefore a key step toward deeper understanding of their performance in applications.

1.1.2 Model uncertainty in stochastic process models

In economics and related research fields, the model uncertainty, often called model ambiguity, has been rigorously evaluated in terms of the risk measure based on the Radon–Nikodym derivative between benchmark and distorted models (Frittelli and Gianin 2004; Föllmer and Knispel 2013; Ben-Tal and Teboulle 2007). Namely, a risk measure evaluates a random quantity of interest through an expectation index distorted according to the worst-case Radon–Nikodym derivative. Major examples of the risk measures are the spectral risk measures including the famous conditional Value-at-Risk (Dowd et al. 2008; Kouri 2019; Guo and Hu 2022) and entropic Value-at-Risk (Ahmadi-Javid 2012), and their generalizations (Zou et al. 2022, 2023).

Risk measures can be systematically studied on the basis of Orlicz spaces: Banach spaces collecting functions equipped with certain growth and regularity conditions

(Rao and Ren 2002; Rubshtein et al. 2016). These spaces are suited to analyzing risk measures as they deal with functions having specific upper- and lower-tail behaviors corresponding to extreme events. Their mathematical rigor enables us to properly understand and quantify the model uncertainty. A convex risk measure and its connection with expected utility theory (Föllmer and Schied 2016) has been widely studied, as an extension of classical Orlicz spaces. Several risk measures including the monetary risk measures (Cheridito and Li 2008, 2009) and entropic Value-at-Risks are defined through norms of Orlicz spaces (Ahmadi-Javid and Pichler 2017). In particular, the Orlicz premia and their robustification have been introduced for studying extreme insurance and financial risks under model uncertainty by directly exploiting the properties of Orlicz spaces (Bellini et al. 2018, 2021; Kong et al. 2018). The Orlicz space suitable for specific random variables such as sub-exponential and sub-Gaussian variables has been studied in Zajkowski (2020). The capital allocation has successfully been studied using the risk measures under Orlicz spaces (Canna et al. 2021; Gómez et al. 2022).

There have been significant advances of the risk measures in Orlicz spaces both in theory and practice as reviewed above, while their applications to stochastic process models of the streamflow discharge do not exist to the best of the authors' knowledge. Moreover, methodologies for efficiently computing the risk measures defined in Orlicz spaces have not been studied well. These two issues motivated the research objective presented below.

1.2 Objective and contribution, and structure of this paper

We have two goals in this paper. The first goal is to formulate a unified mathematical framework based on Orlicz spaces for the statistical evaluation of the model uncertainty of a stochastic process model of the streamflow discharge. The second goal is to apply this framework to real data. In particular, we focus on the mixed moving average process (hereafter called MMA process) as a nominal stochastic process model (Barndorff-Nielsen 2001) recently applied to the discharge time series data having a long memory (Yoshioka 2022). This MMA process is an aggregation of Ornstein–Uhlenbeck type processes and hence generalizes a wide class of existing stochastic process models (e.g., Botter et al. 2013). The aggregation here means the coexistence of multiple time scales in the flow attenuation arising from the spatial averaging of the long- and short-distant runoff processes in the watershed (Mudelsee 2007). The aggregation can be understood through Markovian lifts; a function decaying algebraically is represented as an integration of exponential functions (Cuchiero and Teichmann 2020). The advantage

of the MMA process in applications is that its moments and ACF are obtained in closed forms that are efficiently computable. This property has been inherited in the self-exciting version of the MMA process (Yoshioka et al. 2023). Further, the moments of the MMA process have a common structure that they are determined through integrals of the Lévy measure (a measure governing size and frequency of jumps) and reversion measure (a probability measure to aggregate multiple time scales). Statistical evaluation of the model uncertainty in the MMA process hence reduces to investigations of these two measures.

The conventional risk measures based on Orlicz premia, which we simply call Orlicz risks, have been designed for the evaluation of extreme losses corresponding to upper-tail probabilities considering the decaying speed of the tail. Hence, they are applicable to the estimation of an upper-bound of a statistic, while not only the upper-bound corresponding to flood events but also the lower-bound corresponding to base flows of the discharge (Bahrami et al. 2022; Naqi et al. 2022) are important. We establish a mathematical framework based on a pair of static optimization problems that can consistently cover both the upper- and lower-bounds of statistics of the MMA process based on Orlicz hearts (the space of random variables with which a Orlicz risk is well-defined). The model uncertainty in this framework is evaluated through an entropic risk measure as a functional of a Radon–Nikodym derivative, with which we formulate a class of risk measures to well-define the Orlicz risks. The worst-case uncertainty maximizing/minimizing the random variable of interest would be found from priors in a neighborhood of the benchmark one in the sense of the relative entropy. We employ the Tsallis relative entropy (Tsallis 2009) as a generalized entropic risk measure used in applications ranging from information sciences (Suyari and Tsukada 2005; Tanaka et al. 2015), machine learning (Zimmert and Seldin 2021), and hydrology (Singh et al. 2017); its functional shape especially plays a key role in this paper. More specifically, its regularity property allows us to define Orlicz risks even under the case where the well-known Kullback–Leibler divergence fails. The proposed Orlicz risks are advantageous in applications because they can separately evaluate risks by properly choosing parameters in the Young function and the Tsallis relative entropy.

A limitation of some conventional Orlicz risks is that they assume bounded random variables while those of the stochastic process models of the discharge including the MMA process are unbounded. To overcome this difficulty, the Orlicz heart and the admissible set of model uncertainty are designed in this paper so that the Orlicz risks are well-defined for unbounded random variables. The Orlicz risks are numerically computed by using the dual representation formula based on the Radon–Nikodym derivative (Bellini

et al. 2018). Similarities and differences between the Orlicz risks of the upper- and lower-bounds are discussed focusing on their convexity. We demonstrate that an Orlicz risk can be approximated firstly by discretizing the probability measure and then computing the worst-case Radon–Nikodym derivative by iteratively solving a nonlinear equation. The use of the Tsallis relative entropy allows for explicitly obtaining the Radon–Nikodym derivative, with which the nonlinear equation can be solved efficiently. With our mathematical framework, the risk and uncertainty involved in the streamflow dynamics can be consistently evaluated by specifying few user-dependent parameters. Our theoretical results show that the Orlicz risks can be well-defined (Propositions 1 and 2) and admit desirable ordering properties for evaluating both the risk (Proposition 3) and model uncertainty (Proposition 4).

The proposed Orlicz risks are finally applied to hourly discharge times series data in streamflow environments in Japan. Impacts of model uncertainties on the Lévy and reversion measures are analyzed, and the statistics under the worst-case are evaluated. Consequently, this paper consistently contributes to formulation, analysis, and application of the Orlicz risks with a focus on streamflow environments. Our focus is therefore on the specific time series data, while the framework presented in this paper will be applicable to many other stochastic time series data arising in engineering research fields.

The rest of this paper is structured as follows. Section 2 reviews the MMA process. Section 3 introduces our robust Orlicz risks. Mathematical properties of the Orlicz risks are studied and their computational algorithms are presented in this section. Section 4 studies an application of the Orlicz risks to the discharge data of streamflow environments in Japan. Section 5 presents conclusions and future perspectives of our study. Appendices contain proofs of Propositions that are technical and several auxiliary results.

2 Stochastic process model

2.1 Model formulation

The stochastic process model considered in this paper is the MMA process of the Ornstein–Uhlenbeck type defined on a usual complete probability space $(\Omega, \mathcal{F}, \mathbb{P})$. The formulation in this paper follows that in Barndorff-Nielsen and Stelzer (2013). The MMA process under a stationarity assumption is given as

$$X_t = \int_{-\infty}^{t} \int_{0}^{+\infty} \int_{0}^{+\infty} e^{-r(t-s)} \mu(\mathrm{d}s, \mathrm{d}r, \mathrm{d}z). \tag{1}$$

Here, $t \in \mathbb{R}$ is the time, $X = (X_t)_{t \in \mathbb{R}}$ is the non-negative scalar stochastic process, μ is the Poisson random measure

having the compensator $ds \times \pi(dr) \times v(dz)$ with the infinitesimal time ds, the reversion measure $\pi(dr)$ as a probability measure to aggregate the reversion rate $r > 0$, and the Lévy measure $v(dz)$ of jump size $z > 0$. In (1), the Poisson random measure μ generates jumps that are mutually independent each other, and each jump decays according to the exponential $e^{-r(t-s)}$. The aggregation (integration with respect to r) implies the coexistence of multiple time scales as explained below.

2.2 Statistics

We focus on a long-memory case driven by bounded-variation jumps that are relevant for the discharge time series (Yoshioka 2022; Yoshioka et al. 2023), and hence throughout this paper assume the followings: the reversion measure π admits a probability density and satisfies

$$\int_0^{+\infty} \pi(dr) = 1 \quad \text{and} \quad R := \int_0^{+\infty} \frac{1}{r} \pi(dr) \in (0, +\infty),$$

$$(2)$$

and the Lévy measure $v(dz)$ is absolutely continuous with respect to the Lebesgue measure dz and satisfies

$$\int_0^{+\infty} z v(dz) < +\infty \quad \text{and} \quad \int_{+\varepsilon}^{+\infty} v(dz) < +\infty \quad \text{for each } \varepsilon > 0.$$

$$(3)$$

The condition (2) means that π is a probability measure of a positive random variable and the inverse moment R is bounded. Phenomenologically, R is a macroscopic time-scale of the flow attenuation. The condition (3) implies that the total number of jumps is at most countable in each bounded time interval. If additionally v satisfies $\lambda := \int_0^{+\infty} v(dz) < +\infty$, then each jump follows a compound Poisson process whose jump intensity equals λ. By (3), the probability measure of jumps larger than a prescribed size $\hat{z} > 0$ is given by

$$\frac{1}{\lambda_{\hat{z}}} v(dz) (z > \hat{z}) \quad \text{with} \quad \lambda_{\hat{z}} := \int_{\hat{z}}^{+\infty} v(dz) > 0.$$

$$(4)$$

Here, $\lambda_{\hat{z}}$ is the intensity of jumps larger than $\hat{z}$.

The stationary statistics of the MMA process X are analytically obtained as follows with $\mathbb{E}$ the expectation (e.g., Yoshioka 2022):

$$\text{Mean } \mathbb{E}[X_t] = RM_1, \quad \text{Variance} \quad \mathbb{E}\left[(X_t - \mathbb{E}[X_t])^2\right] = \frac{RM_2}{2},$$

$$(5)$$

Skewness $\dfrac{\mathbb{E}\left[(X_t - \mathbb{E}[X_t])^3\right]}{\mathbb{E}\left[(X_t - \mathbb{E}[X_t])^2\right]^{1.5}} = \dfrac{2\sqrt{2}}{3} \dfrac{1}{\sqrt{R}} \dfrac{M_3}{(M_2)^{3/2}},$

$$(6)$$

Kurtosis $\dfrac{\mathbb{E}\left[(X_t - \mathbb{E}[X_t])^4\right] - 3\mathbb{E}\left[(X_t - \mathbb{E}[X_t])^2\right]^2}{\mathbb{E}\left[(X_t - \mathbb{E}[X_t])^2\right]^2}$

$$= \frac{M_4}{R(M_2)^2},$$

$$(7)$$

where $M_k := \int_0^{+\infty} z^k v(dz) \, (k \in \mathbb{N})$ are moments of the jump size. We also have a closed-form representation of the ACF with time lag $\tau \geq 0$:

$$\rho(\tau) = \frac{1}{R} \int_0^{+\infty} \frac{1}{r} e^{-r\tau} \pi(dr).$$

$$(8)$$

The factors related to Lévy and reversion measures are appearing separately in (5)–(7). Further, by (8) the ACF is free from the Lévy measure.

Remark 1 We focus on the jump-driven MMA process (1), while the ACF (8) has the same form even if we assume an existence of the Gaussian noise (Barndorff–Nielsen 2001). In this case, continuous noise terms will be included in (5)–(7), which are currently under investigations by the authors.

3 Orlicz risks

We formulate and analyze Orlicz risks in this section. All random variables in this section are scalar and positive, and denoted as x. In our application, this x corresponds to the reversion rate r or jump size z. The discussion in this section is rather from a generalized viewpoint, and its adaptations to the specific cases will be considered later (Sect. 3.4).

3.1 Orlicz heart and space

The Orlicz heart and space as a main ingredient of Orlicz risks are defined following Bellini et al. (2018, 2021) (see, also Rao and Ren 2002; Rubshtein et al. 2016). A Young function is a continuous, strictly increasing, and convex function $\Phi : [0, +\infty) \to [0, +\infty)$ such that $\Phi(0) = 0, \Phi(1) = 1$, and $\Phi(+\infty) = +\infty$. Given a probability density $g : [0, +\infty) \to [0, +\infty)$, which is a continuous and measurable function with $\int_0^{+\infty} g(x)dx = 1$, and a Young function Φ, the Orlicz heart $H_{g,\Phi}$ is defined as

$$H_{g,\Phi} := \left\{ f : [0, +\infty) \to [0, +\infty) : \right.$$
$$\left. \int_0^{+\infty} \Phi\left(\frac{f(x)}{k}\right) g(x)\mathrm{d}x < +\infty \text{ for all } k > 0 \right\}. \tag{9}$$

The Orlicz space $L_{g,\Phi}$ is defined as

$$L_{g,\Phi} := \left\{ f : [0, +\infty) \to [0, +\infty) : \right.$$
$$\left. \int_0^{+\infty} \Phi\left(\frac{f(x)}{k}\right) g(x)\mathrm{d}x < +\infty \text{ for some } k > 0 \right\}, \tag{10}$$

and hence $H_{g,\Phi} \subset L_{g,\Phi}$. The Orlicz norm $\|\cdot\|_{g,\Phi}$ is defined for $f \in L_{g,\Phi}$ as

$$\|f\|_{g,\Phi} := \inf\left\{ k > 0 : \int_0^{+\infty} \Phi\left(\frac{f(x)}{k}\right) g(x)\mathrm{d}x \le 1 \right\}. \tag{11}$$

Typical Young functions Φ in the literature are (under the normalization $\Phi(1) = 1$) x^p ($p \ge 1$) and $\frac{\exp(ux^p)-1}{\exp u - 1}$ ($u > 0$, $p \ge 1$) (Rubshtein et al. 2006; Zajkowski 2020). The normalization $\Phi(1) = 1$ is not necessary in general, while it is important for ensuring the consistency between the Orlicz space $L_{g,\Phi}$ and the Lebesgue space L^p in a way that (e.g., Bellini et al. 2018, 2021)

$$\|f\|_p := \left(\int_0^{+\infty} (f(x))^p g(x)\mathrm{d}x \right)^{\frac{1}{p}} = \|f\|_{g,x^p}. \tag{12}$$

This relationship will become important for dealing with the Orlicz risks in this paper.

Remark 2 An Orlicz space as a Banach space should be based on a convex Young function, while defining a Orlicz heart does not require the convexity (Chapter 10. 5 of Rao and Ren 2002). Indeed, we later consider an Orlicz heart with a concave function.

3.2 Tsallis relative entropy

We define the Tsallis relative entropy as another ingredient of the Orlicz risks. The Tsallis relative entropy $D_q(h|g)$ with the shape parameter $q > 0$ of a probability density h with respect to an equivalent probability density g is defined as

$$D_q(h|g) := \begin{cases} \dfrac{1}{1-q}\left(1 - \displaystyle\int_0^{+\infty} \{\phi(x)\}^q g(x)\mathrm{d}x \right) & (q > 0, q \ne 1) \\ \displaystyle\int_0^{+\infty} \phi(x)\ln\phi(x) g(x)\mathrm{d}x & (q = 1) \end{cases}$$
$$\text{for} \quad \int_0^{+\infty} \phi(x)g(x)\mathrm{d}x = 1 \tag{13}$$

with $\phi := h/g$ the Radon–Nikodym derivative that is positive for $x > 0$. Each integrand in D_q is convex with respect to ϕ and is minimized by $\phi(x) = 1$ ($x > 0$). The Tsallis relative entropy D_q reduces to the well-known Kullback–Leibler divergence when $q = 1$. We have $D_q(h|g) \ge 0$ by definition, and $D_q(h|g) = 0$ if and only of $g = h$ for $x > 0$. For the Tsallis relative entropy, a larger q implies a stronger aversion against the model uncertainty (e.g., Ma and Tian 2002; Tian 2023).

We define a q-exponential function and a q-logarithm function used in the sequel:

$$\exp_q(x) = \begin{cases} (1+(1-q)x)^{\frac{1}{1-q}} & (q \ne 1) \\ \exp(x) & (q = 1) \end{cases}, \quad 1+(1-q)x > 0 \tag{14}$$

and

$$\ln_q(x) = \begin{cases} \dfrac{x^{1-q}-1}{1-q} & (q \ne 1) \\ \ln(x) & (q = 1) \end{cases}, \quad x > 0. \tag{15}$$

Both functions are increasing, and $\exp_q$ function is convex while $\ln_q$ function is concave like the classical exp and ln functions, respectively.

3.3 Formulation of Orlicz risks

Upper and lower Orlicz risks serving as the main mathematical tools in this paper are presented. They are formulated in a symmetrical way so that both can be dealt with in a unified manner.

3.3.1 Upper Orlicz risk

The Orlicz risk for the upper-bound, hereafter called upper Orlicz risk, is a specific version of the robust Orlicz premia in Bellini et al. (2018). The upper Orlicz risk $\overline{O}_{g,\Phi_f}$ for $f \in H_{\phi^q g,\Phi}$ ($\phi \in \overline{\mathcal{D}}$) is defined as

$$\overline{O}_{g,\Phi_f} = \inf\left\{ k > 0 : \sup_{\phi \in \overline{\mathcal{D}}}\left\{ \int_0^{+\infty} \Phi\left(\frac{f(x)}{k}\right)\{\phi(x)\}^q g(x)\mathrm{d}x \right.\right.$$
$$\left.\left. - wD_q(\phi g|g) \right\} \le 1 \right\}, \tag{16}$$

where $\overline{\mathcal{D}}$ is an admissible set of Radon–Nikodym derivatives ϕ specified later and $w > 0$ is a weighting factor.

In (16), the first term in the "sup" part is the Orlicz risk premium under the probability density distorted according to the Radon–Nikodym derivative ϕ. The multiplication of the integrand by ϕ^q is due to enforcing the consistency between the risk premium and the penalization by the Tsallis relative entropy D_q as the second term. More

specifically, the coefficient ϕ^q implies that the first term is evaluated under an escort distribution to resolve singular behaviors of the integrands (Chapter 8 of Tsallis 2009): a slow decay for $x \to +\infty$ or a singularity at $x = 0$ in our context. In the second term, the weighting factor w controls the strength of the uncertainty aversion in a way that larger w represents less ambiguous estimate of $\overline{O}_{g,\Phi,f}$. The upper Orlicz risk (16) thus accounts for the risk (first term) and model uncertainty (second term) in a separable manner.

3.3.2 Lower Orlicz risk

The Orlicz risk for the lower-bound, hereafter called lower Orlicz risk, is presented in this sub-section. The distinct difference between the upper and lower Orlicz risks is that the former is defined via a min–max problem while the latter via a max–min problem. In addition, the former uses the Young function Φ that is increasing and convex, while the latter the inverse $\Phi^{(-1)}$ that is increasing and concave. The lower Orlicz risk $\underline{O}_{g,\Phi,f}$ for $f \in H_{\phi^q g, \Phi^{(-1)}}$ ($\phi \in \underline{\mathcal{D}}$) is defined as follows:

$$\underline{O}_{g,\Phi,f} = \sup\{k > 0 :$$
$$\inf_{\phi \in \underline{\mathcal{D}}}\left\{ \int_0^{+\infty} \Phi^{(-1)}\left(\frac{f(x)}{k}\right)\{\phi(x)\}^q g(x)\mathrm{d}x + wD_q(\phi g|g) \right\} \geq 1 \right\},$$
(17)

where $\underline{\mathcal{D}}$ is an admissible set of Radon–Nikodym derivatives ϕ specified later. In (17), the first term in the left-hand side of "inf" part is the Orlicz risk premium under the probability density g distorted according to ϕ in the escort sense. The second term represents the penalization of model uncertainty as in the upper Orlicz risk. The lower Orlicz risk also accounts for the risk (first term) and model uncertainty (second term) in a separable manner.

3.4 Mathematical analysis

The Orlicz risks are mathematically analyzed under assumptions suitable for the application to the Lévy and reversion measures. Propositions 1–2 concern the well-posedness of the upper and lower Orlicz risks, while Propositions 3–4 demonstrate their ordering properties.

3.4.1 Target cases

In this sub-section, we focus on the following specific cases of the triplet (g, Φ, f) that will be considered in our application. For the reversion measure π, we focus on the Gamma density

$$g(r) = g_\pi(r) := \frac{1}{\Gamma(\alpha_\pi)(\beta_\pi)^{\alpha_\pi}} r^{\alpha_\pi - 1} \exp\left(-\frac{r}{\beta_\pi}\right) \text{ for } r > 0$$
(18)

with parameters $\alpha_\pi > 1$ and $\beta_\pi > 0$, where Γ is the Gamma function. We have $R^{-1} = \beta_\pi(\alpha_\pi - 1)$ and $\rho(\tau) = (1 + \beta_\pi r)^{-(\alpha_\pi - 1)}$, the latter being an ACF of an algebraically-decaying process. The process X_t is said to have a long memory if $\rho(\tau)$ is not integrable with respect to the Lebesgue measure $\mathrm{d}\tau$ for $\tau > 0$, which occurs if $\alpha_\pi \in (1, 2]$. The Gamma density is therefore a tractable example of the reversion measure for possibly long-memory processes. For the reversion measure, the function f is $f(r) = r^{-1}$ as our focus is on the inverse moment R in (2).

For the Lévy measure v, we assume the tempered stable one corresponding to the density

$$g(z) = g_v(z) := \frac{\frac{v(\mathrm{d}z)}{\mathrm{d}z}}{\int_{\hat{z}}^{+\infty} v(\mathrm{d}z)}$$
$$= \left\{ \int_{\hat{z}}^{+\infty} \frac{a_v}{z^{\alpha_v + 1}} \exp(-\beta_v z)\mathrm{d}z \right\}^{-1} \frac{a_v}{z^{\alpha_v + 1}} \exp(-\beta_v z)$$
$$\text{for } z > \hat{z}$$
(19)

with parameters $a_v > 0$, $\alpha_v < 1$, and $\beta_v > 0$. In this case, the density g represents the probability density of jump sizes larger than the prescribed threshold $\hat{z} \geq 0$. If $\alpha_v < 0$, then $\hat{z}$ is allowed to be zero because it corresponds to a compound Poisson case, while If $\alpha_v \in [0, 1)$, then $\hat{z}$ must be positive to well-define (19). The latter case corresponds to the situation where the MMA process involves countably infinitely many small jumps in each bounded time interval. For the reversion measure, the function f is $f(z) = z^m$ ($m \in \mathbb{N}$) as our focus is on the jump size.

We must specify the function Φ for specifying the Orlicz risks. We primary consider the power function x^p ($p \geq 1$) unless otherwise specified. In this case, the risk is controlled by the power index p while the uncertainty by the Tsallis relative entropy. With these choice, the risk and uncertainty involved in the streamflow dynamics can be consistently evaluated by specifying few user-dependent parameters: the parameter p representing the ambiguity aversion and the parameters controlling the magnitude w and shape q of the ambiguity aversion.

3.4.2 Upper Orlicz risk

The analysis of upper Orlicz risk is based on Bellini et al. (2018) for the robustified Orlicz risk premia and Ma and Tian (2021) for the Tsallis elative entropy with an adaptation to our setting. Finding the upper Orlicz risk consists of Problems U1 and U2.

Problem U1 *Given the triplet (g, Φ, f) and parameters (q, w), and $k > 0$, solve the maximization problem*

$$G(k) := \sup_{\phi \in \overline{\mathcal{D}}} \left\{ \int_0^{+\infty} \Phi\left(\frac{f(x)}{k}\right) \{\phi(x)\}^q g(x) \mathrm{d}x - w D_q(\phi g | g) \right\}.$$

(20)

Problem U2 *Find a solution $k = \overline{k} > 0$ to the nonlinear equation*

$$G(k) = 1.$$

(21)

We consider Problems U1 and U2 in this order, and then present the well-posedness result of the upper Orlicz risk. We have

$$\int_0^{+\infty} f(x) g(x) \mathrm{d}x \leq \left(\int_0^{+\infty} (f(x))^p g(x) \mathrm{d}x \right)^{\frac{1}{p}}$$
$$= \inf \left\{ k > 0 : \int_0^{+\infty} \Phi\left(\frac{f(x)}{k}\right) g(x) \mathrm{d}x \leq 1 \right\}$$
$$= \overline{O}_{g,\Phi,f}.$$

(22)

A similar inequality applies under uncertainties (Proposition 4).

Problem U1 is just a version of the variational problem dealt with in Sect. 3 of Ma and Tian (2021). Their results suggest that the maximizer $\phi = \overline{\phi}_k$ of (20) is given by

$$\overline{\phi}_k(x) = \left\{ \int_0^{+\infty} \exp_q\left(\frac{1}{w}\Phi\left(\frac{f(x)}{k}\right)\right) g(x) \mathrm{d}x \right\}^{-1} \exp_q\left(\frac{1}{w}\Phi\left(\frac{f(x)}{k}\right)\right) g(x),$$

(23)

and hence the worst-case Radon–Nikodym derivative $\overline{\phi}$ realizing the Orlicz risk by $\overline{\phi} = \overline{\phi}_{\overline{k}}$. We analyze a sufficient condition under which $\overline{\phi}_k$ is well-defined: i.e., the condition where the denominator of (23) is bounded. We should find the condition under which the following Orlicz heart exists:

It also implies a sufficient condition for the existence of (24).

Proposition 1 *Assume the case (i) or (ii) presented below.*

(i) $g(x) = g_\pi(x)$ $(x > 0)$, $f(x) = x^{-1}, p \in (1, \alpha_\pi)$, and $q \in \left(0, 1 - \frac{p}{\alpha_\pi}\right)$. The admissible set $\overline{\mathcal{D}}$ is given by

$$\overline{\mathcal{D}} = \left\{ \phi : (0, +\infty) \to (0, +\infty) | \int_0^{+\infty} \phi(x) g_\pi(x) \mathrm{d}x = 1 \right\}.$$

(25)

(ii) $g(x) = g_v(x + \hat{z})$ $(x > 0)$ with, $p \geq 1$, and $\hat{z} \geq 0, f(x) = x^m$ $(m \in \mathbb{N})$. The threshold $q \in (0, 1)$ $\hat{z}$ is allowed to be 0 only if $\alpha_v < 0$ (Compound Poisson case). The admissible set $\overline{\mathcal{D}}$ is given by (25) with $g_\pi(x)$ replaced by $g_v(x + \hat{z})$.

Then, there exists a unique solution $k = \overline{k} > 0$ to the nonlinear Eq. (21). Furthermore, a maximizer of (20) for $k = \overline{k}$ is $\phi = \overline{\phi}_{\overline{k}}$.

Remark 3 Proposition 1 shows that the Orlicz heart corresponding to the upper Orlicz risk is well-defined if the condition (i) or (ii) is satisfied. Importantly, the case q = 1 where the Tsallis relative entropy reduces to the Kullback–Leibler one is not allowable in (i); indeed, we obtain $G(k) = +\infty$ for all $k > 0$. For the case (ii), if $q = 1$, then the proof for $q \in (0, 1)$ has to be modified because we will need the integrability condition

$$\int_0^{+\infty} \exp\left(\frac{1}{w}\left(\frac{x^m}{k}\right)^p\right) \frac{a_v}{(x + \hat{z})^{\alpha_v + 1}} \exp(-\beta_v(x + \hat{z})) \mathrm{d}x \in (0, +\infty).$$

(26)

This condition is satisfied only if $m = p = 1$ and k is sufficiently large. However, a priori estimate of $\overline{k}$ is not available. In this view, the use of the Tsallis relative entropy is essential in our framework.

$$H_{g, \exp_q\left(\frac{1}{w}\Phi\left(\frac{f(\cdot)}{k}\right)\right)} := \left\{ f : [0, +\infty) \to [0, +\infty) : \int_0^{+\infty} \exp_q\left(\frac{1}{w}\Phi\left(\frac{f(x)}{k}\right)\right) g(x) \mathrm{d}x < +\infty \text{ for all } k > 0 \right\}.$$

(24)

Studying Problem U1 thereby reduces to the analysis of the Orlicz heart (24). After resolving this issue, the unique existence of the solution to Problem U2 follows based on the argument employed in the Proof of Lemma 5 of Bellini et al. (2018).

Proposition 1 below shows the well-posedness of the upper Orlicz risk and further gives the functional shape of the worst-case Radon–Nikodym derivative associated to it.

Remark 4 The admissible set $\overline{\mathcal{D}}$ does not depend on w. It does not depend on p as well for the case (i) as long as $p \in (1, \alpha_\pi)$ or the case (ii) in Proposition 1.

3.4.3 Lower Orlicz risk

We analyze the lower Orlicz risk. The formulation is similar to that in the previous sub-section, but we explain it here for

the sake of self-contentedness of this paper. Finding the lower Orlicz risk consists of Problems D1 and D2.

Problem D1 *Given the triplet (g, Φ, f) and parameters (q, w), and $k > 0$, solve the minimization problem $J(k)$:*

$$= \inf_{\phi \in \underline{\mathcal{D}}} \left\{ \int_0^{+\infty} \Phi^{(-1)}\left(\frac{f(x)}{k}\right) \{\phi(x)\}^q g(x) \mathrm{d}x + w D_q(\phi g | g) \right\}. \tag{27}$$

Problem D2 *Find a solution $k = \underline{k} > 0$ to the nonlinear equation*

$$J(k) = 1. \tag{28}$$

We consider Problems D1 and D2 in this order, and then present the well-posedness result of the lower Orlicz risk. Problem D1 is a minimization version of Problem U1. The use of a concave function $\Phi^{(-1)}$ instead of Φ is due to the Jensen's inequality

$$\int_0^{+\infty} \Phi^{(-1)} f(x) g(x) \mathrm{d}x \leq \Phi^{(-1)}\left(\int_0^{+\infty} f(x) g(x) \mathrm{d}x\right). \tag{29}$$

If $\Phi(x) = x^p$ ($p \geq 1$), then (29) leads to

$$\left(\int_0^{+\infty} (f(x))^{\frac{1}{p}} g(x) \mathrm{d}x\right)^p \leq \int_0^{+\infty} f(x) g(x) \mathrm{d}x. \tag{30}$$

The left-hand side of (30) is the Orlicz premium without uncertainties, given by

$$\sup\left\{ k > 0 : \int_0^{+\infty} \Phi^{(-1)}\left(\frac{f(x)}{k}\right) g(x) \mathrm{d}x \geq 1 \right\}. \tag{31}$$

As $\underline{O}_{g,\Phi,f}$ is not larger than (31), the lower Orlicz risk indeed gives an lower-bound of the expectation of f under g.

As in the previous case, the minimizer $\phi = \underline{\phi}_k$ of (27) should be

$$H_{g,\exp_q\left(-\frac{1}{w}\Phi\left(\frac{f(\cdot)}{k}\right)\right)} := \left\{ f : [0, +\infty) \to [0, +\infty) : \int_0^{+\infty} \exp_q\left(-\frac{1}{w}\Phi^{(-1)}\left(\frac{f(x)}{k}\right)\right) g(x) \mathrm{d}x < +\infty \text{ for all } k > 0 \right\} \tag{33}$$

The lower Orlicz risk is finally obtained as the solution $k = \underline{k}$ to (28).

Studying Problem D1 thereby reduces to the analysis of the Orlicz heart (33) along with a proper admissible set $\underline{\mathcal{D}}$. We state the main result concerning the lower Orlicz risk.

Proposition 2 *Assume the case (i) or (ii) presented below.*

(i) $g(x) = g_\pi(x)$ $(x > 0)$, $f(x) = x^{-1}$, $p \geq 1$, and $q \geq 1$. The admissible set $\underline{\mathcal{D}}$ is given by

$$\underline{\mathcal{D}} = \{\phi : (0, +\infty) \to (0, +\infty) | \int_0^{+\infty} \phi(x) g_\pi(x) \mathrm{d}x = 1\} (= \overline{\mathcal{D}}). \tag{34}$$

(ii) $g(x) = g_v(x + \hat{z})$ $(x > 0)$ with $\hat{z} \geq 0$, $f(x) = x^m$ $(m \in \mathbb{N})$, $p \geq 1$, and $q \geq 1$. The threshold $\hat{z}$ is allowed to be 0 only if $\alpha_v < 0$. The admissible set $\underline{\mathcal{D}}$ is given by (34) with $g_\pi(x)$ replaced by $g_v(x + \hat{z})$.

Then, there exists a unique solution $k = \underline{k} > 0$ to the nonlinear Eq. (28). Furthermore, a minimizer of (27) for $k = \underline{k}$ is $\phi = \underline{\phi}_k$.

Remark 5 Proposition 2 shows that the singularity issue encountered at $q = 1$ in Proposition 1 does not occur for the lower Orlicz risk. Instead, we must have $q \geq 1$ for its well-posedness.

$$\underline{\phi}_k(x) = \left\{ \int_0^{+\infty} \exp_q\left(-\frac{1}{w}\Phi^{(-1)}\left(\frac{f(x)}{k}\right)\right) g(x) \mathrm{d}x \right\}^{-1} \exp_q\left(-\frac{1}{w}\Phi^{(-1)}\left(\frac{f(x)}{k}\right)\right) g(x), \tag{32}$$

and hence the worst-case Radon–Nikodym derivative by $\phi = \underline{\phi}_k$. We have to consider a sufficient condition under which $\underline{\phi}_k$ is well-defined: i.e., the condition where the denominator of (32) is bounded. It means that we need to find the condition under which the following specific Orlicz heart exists:

3.4.4 Ordering properties

We show that the proposed Orlicz risks serve as risk measures under uncertainty owing to certain ordering properties. Proposition 3 below shows that the upper and lower Orlicz risks indeed give upper- and lower-bounds of the random variable of interest.

Proposition 3 *The following (a) and (b) hold true.*

(a) *Assume that either the conditions (i) or (ii) of Proposition 1 is satisfied. Then, for $0 < w_1 \le w_2$ it follows that*

$$\int_0^{+\infty} f(x)g(x)\mathrm{d}x \le \left(\int_0^{+\infty} (f(x))^p g(x)\mathrm{d}x \right)^{\frac{1}{p}} \tag{35}$$
$$\le \overline{O}_{g,\Phi f}\big|_{w=w_2} \le \overline{O}_{g,\Phi f}\big|_{w=w_1}.$$

(b) *Assume that either the conditions (i) or (ii) of Proposition 2 is satisfied. Then, for $0 < w_1 \le w_2$ it follows that*

$$0 < \underline{O}_{g,\Phi f}\big|_{w=w_1} \le \underline{O}_{g,\Phi f}\big|_{w=w_2} \le \left(\int_0^{+\infty} (f(x))^{\frac{1}{p}} g(x)\mathrm{d}x \right)^p \le \int_0^{+\infty} f(x)g(x)\mathrm{d}x. \tag{36}$$

The last theoretical results are ordering properties with respect to the power p, showing that it serves as a parameter controlling the risk aversion in the statistical evaluation. Proposition4 below shows that, as a rule of thumb, the target statistic is evaluated to be larger (resp., smaller) as p becomes larger than 1 (resp., smaller than 1) irrespective to the existence or absence of the uncertainty.

Proposition 4 *The following (a) and (b) hold true.*

(a) *Assume that either the conditions (i) or (ii) of Proposition 1 is satisfied for $p = p_1, p_2$ with $1 \le p_1 \le p_2$. Then, it follows that*

$$\overline{O}_{g,\Phi f}\big|_{p=p_1} \le \overline{O}_{g,\Phi f}\big|_{p=p_2}. \tag{37}$$

(b) *Assume that either the conditions (i) or (ii) of Proposition 2 is satisfied for $p = p_1, p_2$ with $1 \le p_1 \le p_2$. Then, it follows that*

$$0 < \min\left\{ 1, \left(w\frac{1}{q-1} \right)^{p_2 - p_1} \right\} \times \underline{O}_{g,\Phi f}\big|_{p=p_2} \le \underline{O}_{g,\Phi f}\big|_{p=p_1}. \tag{38}$$

Remark 6 In Proposition 4, the factor multiplied by $\underline{O}_{g,\Phi f}\big|_{p=p_2}$ is due to the technical assumption, which becomes less if the uncertainty is anticipated to be smaller ($w >> 1$).

3.5 Numerical algorithm

We compute the Orlicz risks using an iterative numerical algorithm explained below. We present only the algorithm to find $\overline{O}_{g,\Phi f}$ here, while that for $\underline{O}_{g,\Phi f}$ can be developed in a similar way (Algorithm 2 in Appendix C in Supplementary material). Algorithm 1 below aims at computing the upper-Orlicz risk $\overline{O}_{g,\Phi f}$ and the associated worst-case Radon–Nikodym derivative $\overline{\phi}$ for the specific choice $\Phi(x) = x^p (p \ge 1)$. The super-script "$(\cdot)$" counts the iteration starting from 0. We exploit the dual representation (e.g., Example 9 in Bellini et al. 2021)

$$\overline{O}_{g,\Phi f} = \sup_{\phi \in \overline{\mathcal{D}}} \left(\frac{\int_0^{+\infty} (f(x))^p \{\phi(x)\}^q g(x)\mathrm{d}x}{1 + wD_q(\phi g|g)} \right)^{\frac{1}{p}}. \tag{39}$$

Algorithm 1

1. Set g, Φ, f and the weighting factor w.
2. Set the initial guess $\overline{\phi}^{(0)}(x) = 1$ $(x > 0)$ and $\overline{k}^{(0)} > 0$.
3. Set the iteration count $m = 0$.
4. Compute

$$\overline{\phi}^{(m+1)}(x) = \left\{ \int_0^{+\infty} \exp_q\left(\frac{1}{w} \left(\frac{f(x)}{\overline{k}^{(m)}} \right)^p \right) g(x)\mathrm{d}x \right\}^{-1}$$
$$\exp_q\left(\frac{1}{w} \left(\frac{f(x)}{\overline{k}^{(m)}} \right)^p \right)$$

.

5. Compute

$$\overline{k}^{(m+1)} = \left\{ \frac{\int_0^{+\infty} (f(x))^p \left\{ \overline{\phi}^{(m+1)} \right\}^q g(x)\mathrm{d}x}{1 + wD_q\left(\overline{\phi}^{(m+1)} g \middle| g \right)} \right\}^{\frac{1}{p}}$$

.

6. If $\left| \overline{\phi}^{(m+1)} - \overline{\phi}^{(m)} \right| \le \text{Err}$, then output $\overline{k}^{(m+1)}$ as the approximation of $\overline{O}_{g,\Phi f}$ and $\overline{\phi}^{(m+1)}$ as the approximation of $\overline{\phi}$, and go to 7. If it is not, set $m \to m+1$ and go to 4.
7. Terminate the algorithm.

Algorithm 1 is a simple fixed-point iteration. Implementation of Algorithm 1 requires some numerical quadrature for the integrals. We use the adaptive quantile discretization (Yoshioka and Yoshioka 2023) and Step 6 is evaluated at all grid points with the degree-of-freedom of $2^{17} = 131,072$. The error threshold Err is 10^{-9}. In Sect. 4, each computation of an Orlicz risk terminates with less
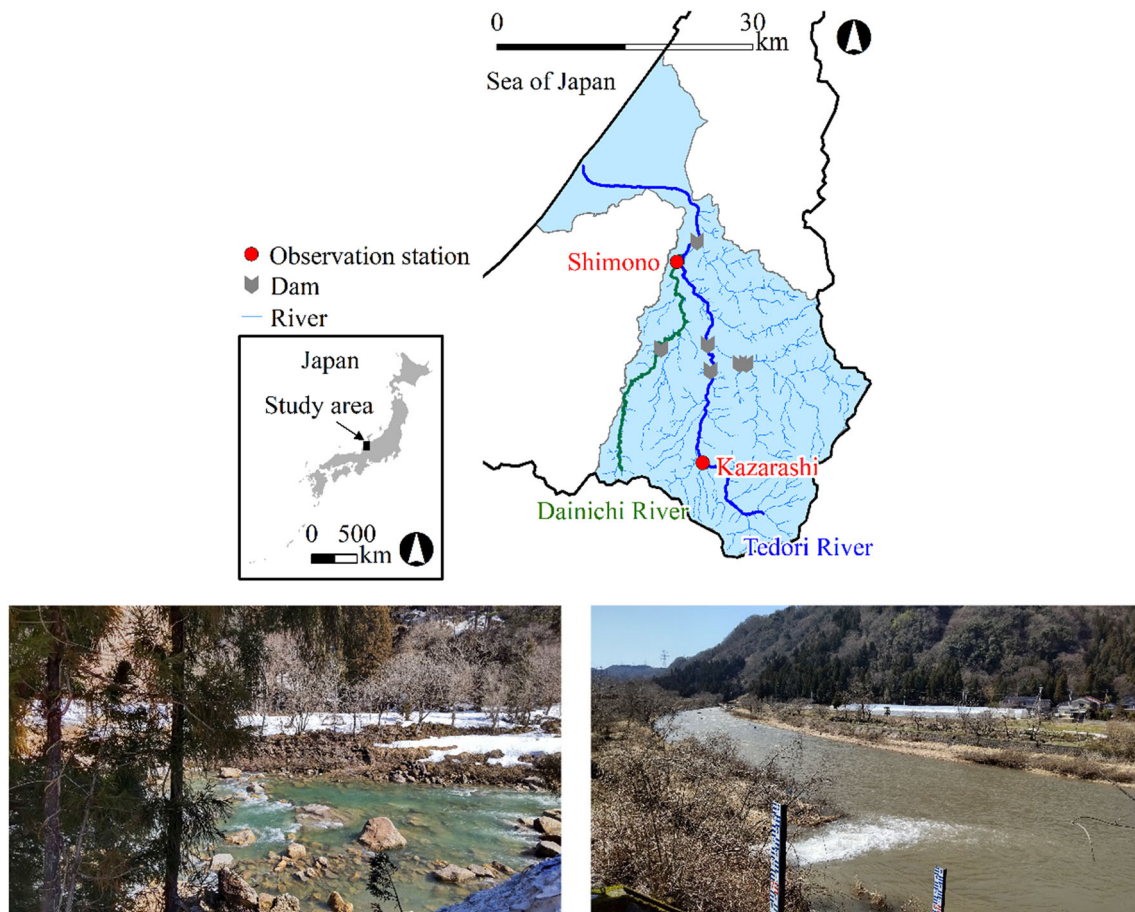
Fig. 1 Map of the study area (up) and photos around Kazarashi (bottom left) and Shimono (bottom right) taken on March 14, 2023 by Hidekazu Yoshioka

than 10 iterations of Steps 5 through 7 in Algorithm 1 in most cases. The computational time of each computation for an Orlicz risk with a common laptop is less than one second. These algorithms further benefit from the closed-form availability of $\overline{\phi}_k, \underline{\phi}_k$ that are with which each integral can be evaluated efficiently.

4 Applications

4.1 Study site

The study site for the application of the Orlicz risks is the Tedori River in Ishikawa Prefecture, Hokuriku Region, Japan (Fig. 1). The explanation of the Tedori River follows Yoshioka et al. (2020) who studied the regional hydrological characteristics around this river. The upstream-end of the Tedori River is in the Hakusan Mountains at the maximum elevation of 2702 (m) and the river pours to the Sea of Japan. The length of the main branch of the Tedori River is 72 (km) and its watershed area is 807 (km^2). There

exists a fan area with the area of 191 (km^2) and the apex height of 80 (m) in the downstream part of the Tedori River. This fan area is a major rice-producing area in Japan whose irrigation water depends on the flowing water of the Tedori River and the groundwater in the shallow aquifer extending around the river. Evaluation of the streamflow environments of the Tedori River as a source of water for the agriculture and regional water environment is therefore an important engineering topic. Moreover, the Tedori River has a series of cascading dams consisting of the Tedori Dam whose operations have been discussed for the flood control (Yuhi 2008), suggesting that studying the river is also important from the viewpoint of disaster management. In this paper, we also consider the data of the Dainichi River as a southern branch of the Tedori River also having a dam called Dainich-gawa Dam for irrigation, hydropower generation, and flood control. This is because the data at the main branch of the Tedori River and the Dainichi River turn out to be qualitatively different from each other in view of the reversion measures as shown later.

Fig. 2 Hourly streamflow discharge data at Kazarashi (red) and Shimono (blue)
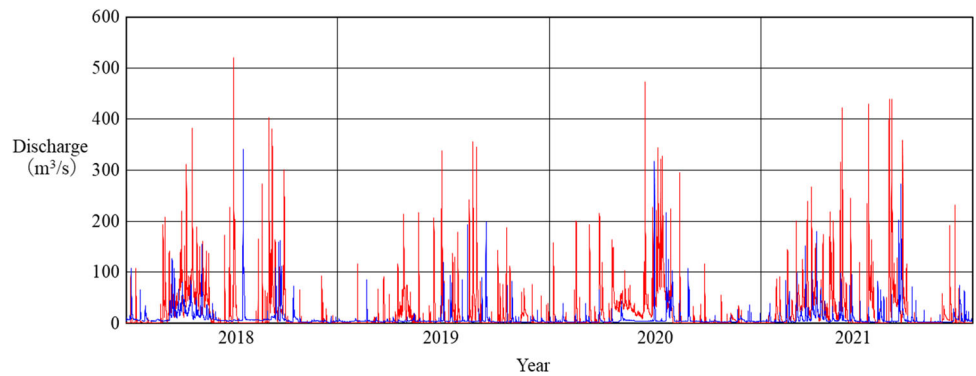
4.2 Identification of the nominal model

The hourly time series data of the streamflow discharge is available at several points in the Tedori River system in the public database provided by Ministry of Land, Infrastructure, Transport and Tourism (2023). We have chosen the two observations stations in this paper, which are Kazarashi (136°37′55″ E, 36°10′04″ N) in the main branch of the Tedori River and Shimono (136°36′10″ E, 36°22′50″ N) in the Dainichi River. Both stations are in the mountainous region of the watershed of the Tedori River (Fig. 1). Both observation stations are in the major recreational fishing area in the Hakusan Mountains, hence analyzing their hydrological characteristics are also of importance from fisheries standpoints. We use the four-year (1461 (day) or equivalently 35,064 (hour)) latest available data set from January 1 2018 01:00:00 JST to December 31 2021 24:00:00 JST (Fig. 2). The total number of the hourly data available at Kazarashi and Shimono during the target period are 35,063 and 34,886, respectively, except for the missing values.

We identify the MMA process, namely the Lévy and reversion measures at the two observation stations. The identification method used here is based on the moment matching method of Yoshioka (2023) assuming a stationary state of the discharge, while the seasonality including the snow-induced runoffs and typhoon-induced floods exist in the study area (Noto et al. 2013). We therefore extend their method to the time series having a seasonality. The discharge data at time t is denoted as Q_t. We assume that there is a positive and time-periodic deterministic quantity s_t having the period T (365.25 (day)), such that there exists an MMA process X_t satisfying

$$Q_t = S_t X_t \text{ or equivalently } \ln Q_t = \ln S_t + \ln X_t. \quad (40)$$

The left-hand side of (40) is available as it is the time series data itself, while the left-hand side is not. This parameterization effectively preserves the statistical characteristics (5)–(8) of the MMA process X_t into the discharge Q_t

Table 1 Parameters of the seasonal component S_t (θ_1, θ_2 are $[0, 2\pi]$ (rad))

	Kazarashi	Shimono
A (m³/s)	1.313	1.657
η_1 (m³/s)	− 0.6341	− 0.4406
η_2 (m³/s)	− 1.601	− 0.8762
θ_1 (rad)	0.9840	0.4636
θ_2 (rad)	2.920	3.134

Table 2 Parameters of the Lévy and reversion measures of X_t

	Kazarashi	Shimono
a_v (1/h)	0.006808	0.009774
α_v (−)	0.05886	0.2770
β_v (−)	0.01928	0.07380
α_π (−)	1.716	2.105
β_π (1/h)	0.09368	0.04616
R (h)	14.90	19.61

because S_t is deterministic and varies slowly compared to X_t, and the relationship (40) is a simple multiplication.

We firstly identify S_t ($t = 0$ is January 1 2018 01:00:00 JST) by applying the classical least-squares method to minimize the empirical time average

$$\frac{1}{N} \sum_{i=1}^{N} (\ln Q_t - \ln S_t)^2, \quad (41)$$

where N is the total number of data points. We parameterize S_t as follows, which has preliminary been found to work reasonably well:

$$\ln S_t = A + \eta_1 \sin\left(\frac{2\pi t}{T} + \theta_1\right) + \eta_2 \sin^3\left(\frac{2\pi t}{T} + \theta_2\right) \quad (42)$$

with parameters $A, \eta_1, \eta_2, \theta_1, \theta_2$ and non-italic π in (42) is the circle ratio (3.14159…). After identifying S_t, we recover X_t as $X_t = Q_t/S_t$, and apply the identification method of Yoshioka et al. (2023) to this X_t; i.e., the
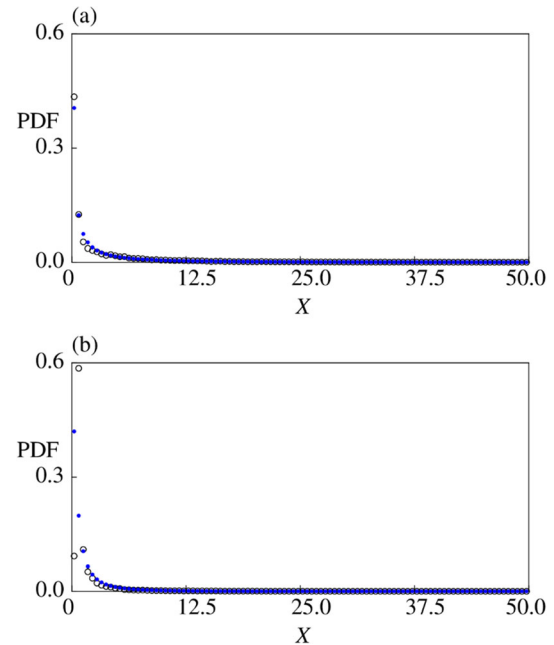
Table 3 Empirical and fitted statistics of the MMA process X_t

	Kazarashi			Shimono		
	Empirical	Fitted	Relative error	Empirical	Fitted	Relative error
Average	4.3333	4.3277	0.0013070	1.6076	1.5937	0.0086696
Variance	105.54	105.61	0.00065220	7.7728	7.8061	0.0042792
Skewness	6.5914	6.5303	0.0092631	6.0522	5.5706	0.079574
Kurtosis	72.407	72.691	0.003920943	53.496	55.173	0.031351
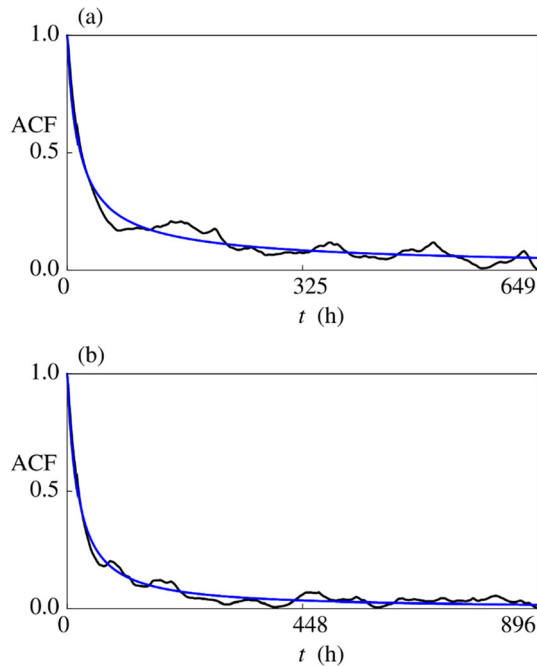
Fig. 3 Comparison between empirical and theoretical ACFs: **a** Kazarashi and **b** Shimono. The empirical and fitted values are represented by black and blue, respectively

Fig. 4 Comparison between empirical and theoretical PDFs in an ordinary scale: **a** Kazarashi and **b** Shimono. The empirical and fitted values are represented by black and blue, respectively

reversion measure π is identified by a least-square fitting between empirical and theoretical ACFs, and then the Lévy measure ν by a minimization of the sum of the squares of the relative errors of the average, variance, skewness, and kurtosis between empirical and theoretical ones.

Tables 1 and 2 show the fitted parameter values of the seasonal component S_t and MMA process X_t at each station, respectively (see, also Appendix B in Supplementary material). Table 3 compares the empirical and theoretical average, variance, skewness, and kurtosis. According to Table 3, moments of the MMA process are reproduced within the relative error at most few % by the fitted model; in particular, the relative errors of the mean and variance are less than 1% for both stations. Figure 3 demonstrates that the reversion measure of the Gamma type (18) is suitable for the streamflow discharge data. The parameter values of the MMA process in Table 2 suggest two differences between the two stations. Firstly, on the Lévy measure ν, the driving jumps at Kazarashi are closer to

compound-Poisson type having finite activities ($\alpha_\nu \geq 0$ but $\alpha_\nu \simeq 0$), while that at Shimono have infinite activities ($\alpha_\nu \geq 0$). Secondly, on the reversion measure π, the MMA process at Kazarashi has a long memory ($\alpha_\pi \in (1, 2]$), while that at Shimono is not ($\alpha_\pi \in (2, +\infty)$). The fitted models thus suggest that the streamflow discharge at Kazarashi is driven by less frequent floods that persist longer than that at Shimono. This difference is considered due to that the Kazarashi and Shimono have different catchments with each other because the former is at the main branch of the Tedori River, while the latter at its tributary. More detailed discussion would require deeper hydrological analysis of the groundwater and surface water of these watersheds that is beyond the scope of this paper.

Figure 4 compares the empirical and fitted stationary probability density functions (PDFs) of the MMA process at each station to check the performance of the identified models. The PDFs of the fitted model were computed by the Monte-Carlo method (Yoshioka et al. 2022). The empirical and fitted result agree reasonably well at both
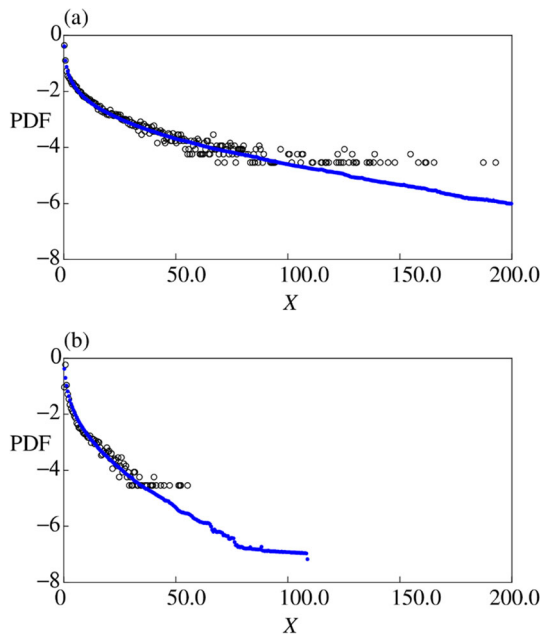
Fig. 5 Comparison between empirical and theoretical PDFs in a logarithmic scale: **a** Kazarashi and **b** Shimono. The empirical data and model result are represented by black and blue, respectively

Fig. 6 Pareto frontiers $(\underline{D}(w), \underline{O}(w))$ at **a** Kazarashi and **b** Shimono

stations. Figure 5 for the PDFs in the logarithmic scale demonstrates that the fitted models capture the tails of the empirical results. The scattering of the tails of the PDFs for large X is due to that the data of flood events rare limited, implying that this part contributes to the model uncertainty. Note that Yoshioka and Yoshioka (2023) also pointed out the long-memory property of the discharge at Kazarashi, but their method assumed the stationarity ($S_t = 1$ in our context). Our results suggest that the proposed de-seasonalization method (40) preserves these properties of the original data.

4.3 Orlicz risks

Upper and lower Orlicz risks are computed at the two observation stations. We especially focus on the two aspects of the streamflow discharge. The first aspect is the base flow and the flow attenuation or persistence, which can be captured by the reversion measure π. The lower Orlicz risk then serves as a lower-bound of the based flow and the attenuation speed. The second aspect is the size and frequency of floods shaped by the Lévy measure v. The upper Orlicz risk then serves as an upper-bound of the size or frequency of floods conditioned on jumps larger than the threshold value $\hat{z}$. In what follows, the subscript "g, Φ, f" is omitted from the Orlicz risks $\overline{O}_{g, \Phi, f}$ and $\underline{O}_{g, \Phi, f}$ for sake of simplicity. The Tsallis relative entropy with $\phi = \overline{\phi}$ and $\phi = \underline{\phi}$ are denoted as $\overline{D}$ and $\underline{D}$ in what follows. We then discuss the pareto frontier by using the couple $(\overline{D}, \overline{O}) =$
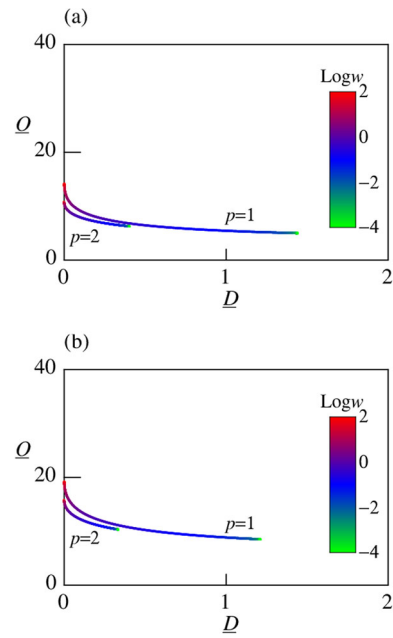
$(\overline{D}(w), \overline{O}(w))$ or $(\underline{D}(w), \underline{O}(w))$ with the weighting factor w being a parameter.

Figure 6 shows the pareto frontiers $(\underline{D}(w), \underline{O}(w))$ at Kazarashi (Fig. 6a) and Shimono (Fig. 6b) with $(g, \Phi, f) = (\pi, x^p, x^{-1})$. We examine $p = 1$ and $p = 2$ to analyze impacts of the risk aversion. Figure 7 plots the corresponding worst-case Radon–Nikodym derivatives $\underline{\phi}$ at Kazarashi. The shape parameter q is set as 1.5. The worst-case Radon–Nikodym derivatives at Shimono are not presented here because these are similar to that presented in Fig. 7. In the present cases, the lower Orlicz risk $\underline{O}$ corresponds to the lower estimate of the time scale R of the flow attenuation.

Figure 6 implies that, at both stations, the lower Orlicz risk $\underline{O}$ for R decreases as the Tsallis relative entropy $\underline{D}$, namely the model uncertainty increases. This result is intuitive as anticipating a larger uncertainty would give a more pessimistic result. Comparing the pareto frontiers between $p = 1$ and $p = 2$ shows that the frontier with $p = 2$ is placed below that with $p = 1$ and they do not intersect with each other. This is the consequence of the stronger risk aversion with $p = 2$ than $p = 1$, while it should also be pointed out that the relative entropy $\underline{D}$ is smaller for the more risk-averse case p = 2 at both stations. This finding implies an interaction between the risk and uncertainty that the more-risk averse estimation of the Orlicz risk would associates a smaller maximum uncertainty possibly due to the stronger precautionary behavior inherent in the Orlicz
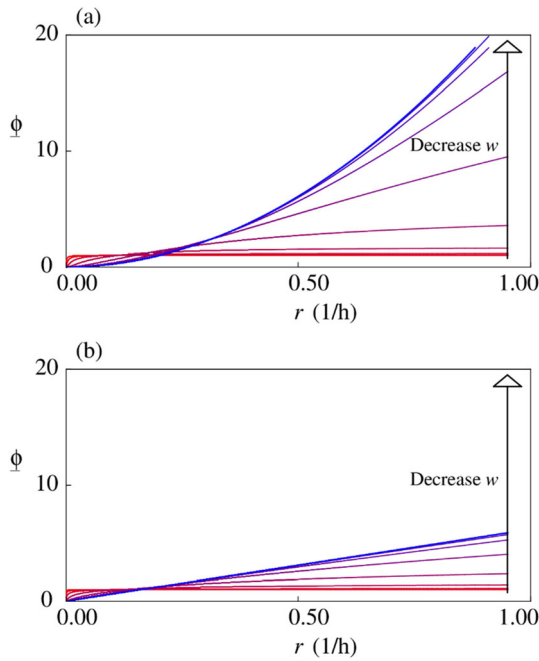
Fig. 7 Worst-case Radon–Nikodym derivatives at Kazarashi: **a** $p = 1$ and **b** $p = 2$. The values of the weight are $w = 10^{2-4i/10}$ $(i = 0, 1, 2, \ldots, 10)$ (see the arrow in the figure)
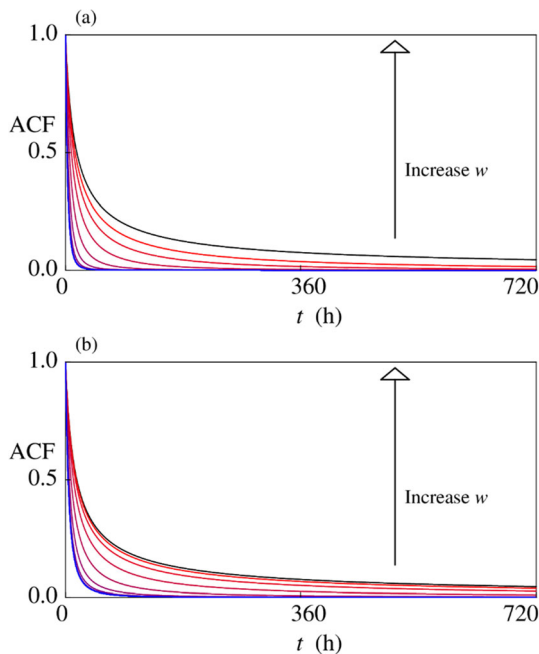

Fig. 8 The ACFs distorted by the worst-case Radon–Nikodym derivative at Kazarashi: **a** $p = 1$ and **b** $p = 2$. The values of the weight are $w = +\infty$ (no uncertainty) and $w = 10^{2-4i/10}$ $(i = 0, 1, 2, \ldots, 10)$ (see the arrow in the figure)

risk. Another interesting finding is that the right-end of the pareto frontier of $p = 1$ is placed below that of $p = 2$; e.g., $4.94 = \underline{O}|_{p=1,w=10^{-4}} < \underline{O}|_{p=0.5,w=10^{-4}} = 6.22$ at Kazarashi. In
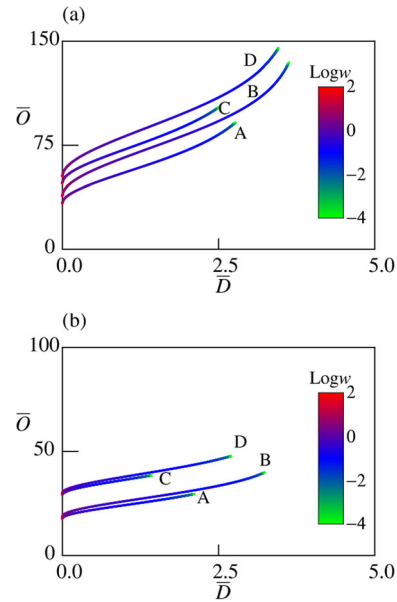
Fig. 9 Pareto frontiers $(\overline{D}(w), \overline{O}(w))$ at **a** Kazarashi and **b** Shimono. Here, the legends A through D in each figure panel represent the couple $(p, \hat{z})$ as follows: A (1, 10), B (1.5, 10), C (1, 20), and D (1.5, 20)

fact, we empirically found that there exists a lower-bound of the Tsallis relative entropy $\lim_{w \to +0} \underline{D}$, which is almost attained at $w = 10^{-4}$ in our computational experiment. The obtained results imply that a smaller uncertainty is allowed to exist for a more risk-averse estimation when the uncertainty is evaluated through the Tsallis relative entropy.

A comparison between Fig. 6a, b implies the larger uncertainty in terms of the Tsallis relative entropy at Kazarashi than Shimono, the former admits a longer memory structure and hence a stronger persistence of fluctuation in the time series data. We focus on the model at Kazarashi having the long memory, and analyze how the ACF can be distorted. Figure 7 shows the worst-case Radon–Nikodym derivatives against different values of p. The growth speed of $\underline{\phi}$ is at most polynomial and saturates at high r as theoretically inferred from the representation (32). Figure 8 shows the corresponding ACF distorted by the worst-case Radon–Nikodym derivative, which is defined as

$$\rho(\tau) = \left(\int_0^{+\infty} \frac{1}{r} \left\{ \underline{\phi}(r) \right\}^q \pi(\mathrm{d}r) \right)^{-1} \int_0^{+\infty} \frac{1}{r} e^{-r\tau} \left\{ \underline{\phi}(r) \right\}^q \pi(\mathrm{d}r) \tag{43}$$

because the reversion measure π is distorted by $\underline{\phi}$. Figure 8 suggests that the lower estimation of the time scale R results in the faster decay of the ACF, meaning that the flow attenuation is estimated to be faster. This is due to the more variable $\underline{\phi}$ for the case p = 1 than $p > 1$ as visually
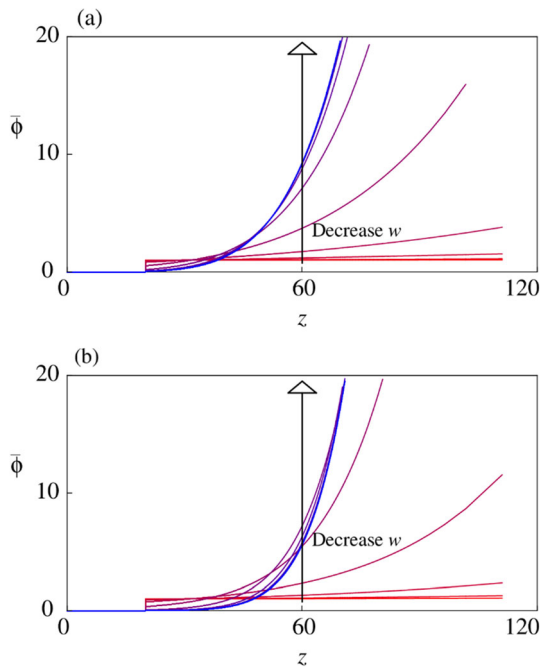
Fig. 10 Worst-case Radon–Nikodym derivatives at Shimono: **a** $p = 1$ and **b** $p = 1.5$. The values of the weight are $w = 10^{2-4i/10}$ ($i = 0, 1, 2, \ldots, 10$) from the top to the bottom

implied in Fig. 7. Consequently, for the same value of the weight w, the impacts of the model uncertainty on the ACF are larger for the smaller p.

Figure 9 shows the pareto frontiers $\left(\overline{D}(w), \overline{O}(w)\right)$ at Kazarashi (Fig. 9a) and Shimono (Fig. 9b) with

$$(g, \Phi, f) = \left(\frac{\mathbb{1}_{(x > \hat{z})} v(\mathrm{d}x)}{\int_{\hat{z}}^{+\infty} v(\mathrm{d}x)}, x^p, x \right)$$

. We examine $p = 1$ and $p = 1.5$ to analyze the impacts of the risk aversion. Figure 10 plots the corresponding worst-case Radon–Nikodym derivatives $\overline{\phi}$ at Kazarashi. The shape parameter q is set as 0.8. In the present case, the upper Orlicz risk $\overline{O}$ corresponds to the upper estimate of the average of jump size conditioned on jumps larger than $\hat{z}$. Considering the parameter values A, η_1, η_2 in Table 1, the magnitude of S_t is around $O(10^0)$ to $O(10^1)$ (m³/s). The threshold values $\hat{z} = O(10^1)$ are therefore analyzed in this paper as it corresponds to floods with the discharge $O(10^1)$ to $O(10^2)$ (m³/s) moderately observed in the real data while significantly larger than the base flow (1–2 (m³/s)) at both stations.

Figure 9 suggests that the higher-risk aversion with higher p results in a larger upper Orlicz risk $\overline{O}$ given the uncertainty $\overline{D}$. This observation applies to the different values of the threshold $\hat{z}$ at both stations. The conditional Jump sizes are larger at Kazarashi than at Shimono for both
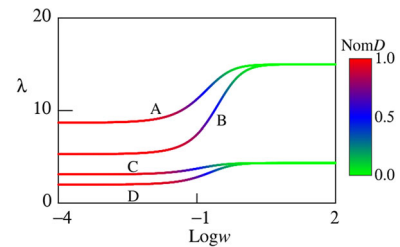
Fig. 11 The frequency λ subject to the distortion at Shimono. Here, the legends A through D represent the couple $(p, \hat{z})$ as follows: A (1, 10), B (1.5, 10), C (1, 20), and D (1.5, 20). "Nom$D$" in the figure is the normalized $\overline{D}$ valued in [0, 1] given by $\mathrm{Nom}D = \overline{D}/\overline{D}\big|_{w=10^{-4}}$

threshold values $\hat{z} = 10$ and $\hat{z} = 20$, while it should be noted that the jumps are now non-dimensional because the MMA process is a non-dimensionalized as well as de-seasonalized quantity as shown in (40). Figure 10 shows the worst-case Radon–Nikodym derivative for $\hat{z} = 20$ against different values of p, demonstrating that they increase sharply with respect to z for the larger p being consistent with the formula (23).

We now focus on the model at Shimono and analyze how the frequency of the event $z > \hat{z}$ is distorted due to the Radon–Nikodym derivative. Here, the frequency of the event $z > \hat{z}$ subject to the distortion, simply denoted as λ, is

$$\lambda = \int_{\hat{z}}^{+\infty} \left\{ \overline{\phi}(z) \right\}^q v(\mathrm{d}z). \tag{44}$$

This λ under no uncertainty and no risk aversion is 13.7 (1/year) for $\hat{z} = 10$ and 3.52 (1/year) for $\hat{z} = 20$. Figure 11 shows the frequency λ computed according to (44), showing that λ decreases as the weight w decreases or equivalently as the uncertainty $\overline{D}$ increases. This finding combined with Fig. 9 shows that under the risk-aversion and/or model uncertainty, the flood frequency decreases while the flood size increases. The degree of the decrease of the flood frequency is bounded from below even when the weight w becomes small due to the boundedness of the uncertainty $\overline{D}$. Both stations have similar shapes of the pareto frontier, while that of Kazarashi results in the larger Orlicz risk reflecting the more frequent as well as larger jumps as shown in Fig. 2.

As demonstrated in the application study of this paper, the proposed Orlicz risks themselves and the associated statistical quantities such as the worst-case Radon–Nikodym derivative and the Tsallis relative entropy can be effectively utilized for the evaluation of the streamflow discharge in a mathematically rigorous as well as computational feasible way.

As an advanced topic, we finally apply the Orlicz risks with a non-polynomial $\Phi(x) = \frac{\exp(ux)-1}{\exp u-1}$ with the parameter of risk aversion $u > 0$ to demonstrate that our framework is
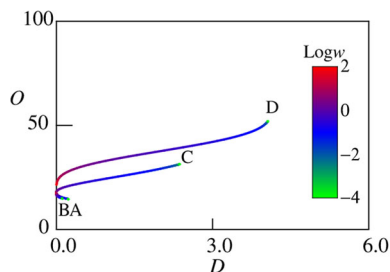
Fig. 12 Pareto frontiers $(D(w), O(w))$ and at Shimono. The legends A through D represent the cases as follows: A $(\underline{D}(w), \underline{O}(w))$ with $u = 0.1$, B $(\underline{D}(w), \underline{O}(w))$ with $u = 1$, C $(\overline{D}(w), \overline{O}(w))$ with $u = 0.1$, and D $(\overline{D}(w), \overline{O}(w))$ with $u = 1$

applicable to Φ other than x^p. We compute the upper and lower Orlicz risks for the triplet (g, Φ, f) employed in the previous sub-section to compute the distorted jump size at Shimono. We use $\hat{z} = 10$ and $u = 0.1$ or $u = 1$. The exponential Young function grows more rapidly than the polynomial one, and hence incurs a stronger risk aversion. Indeed, in this case, the Orlicz space and Orlicz heart are not identical with each other due to

$$\int_0^{+\infty} \Phi\left(\frac{f(x)}{k}\right) g(x) \mathrm{d}x = \int_0^{+\infty} \frac{\exp\left(\frac{ux}{k}\right) - 1}{\exp u - 1} g_v(x) \mathrm{d}x$$
$$= +\infty \tag{45}$$
$$\text{if} \quad \frac{u}{k} > \beta_v.$$

This is contrasting to the case $\Phi(x) = x^p$ studied above where the left-most side of (45) is bounded for all $k > 0$.

Algorithms 1 and 2 do not apply in the present case because the analytical formula like (39) is not available. We therefore employ Algorithms 3 and 4 presented in Appendix C Supplementary material, which do not rely on (39) but employ an additional loop to iteratively update the optimal $\overline{k}, \underline{k}$. The computational costs thereby increase in this case, while its efficiency improvement is beyond the scope of this paper. Figure 12 demonstrates that both the upper and lower Orlicz risks are computed as in the previous cases. For the lower Orlicz risks, the results with $u = 0.1$ and $u = 1$ overlap although the latter results in the smaller estimate along with the larger uncertainty. By contrast, for the lower Orlicz risks, the two cases $u = 0.1$ and $u = 1$ are clearly separated. In particular, the right-end of the curve "D" in Fig. 12 reaches the higher risk than the curves "A" and "B" in Fig. 9b for the polynomial Φ, suggesting the larger risk aversion of the present exponential one. Other choices of Φ would work as well, while choosing a very rapidly increasing Φ fails the convergence of Algorithm 3, also highlighting its stability restriction.

5 Conclusion

We proposed Orlicz risks under model uncertainty with a focus on their applications to stochastic process models of the streamflow discharge. The proper conditions to well-define the upper and lower Orlicz risks were obtained along with their ordering properties. The application of the Orlicz risks to the streamflow discharge data at observation stations in a river system in Japan suggested that they potentially serve as effective risk measures to statistically evaluate the MMA process. Due to the generality of the presented framework, it can also be applied to the other stochastic phenomena such as the rainfall as a point process (Hottovy and Stechmann 2023) with a proper modification of the system dynamics.

Our application concerned the risk evaluation of static random variables, while dynamic ones are also of great importance in real problems. The dynamic Orlicz risks (Bellini et al. 2021) would be a good starting point to deal with such an extended problem. Comparison of the robustified Orlicz risks against other risk measures, such as the conditional Value-at-Risk and spectral risk measures as its generalization (Wei et al. 2022; Wang and Chapman 2022) in the dynamic case will be an interesting topic. Investigations of the Orlicz risks with more generic Young functions will also be interesting, where the development of an efficient computational method will become a key issue as the analytical formulae used in our algorithms may not apply. In particular, the asymptotic behavior of Young functions should be carefully analyzed depending on the problems of interest. We are currently investigating a dynamic Orlicz risk suited to a sustainability assessment of an environmental restoration problem of river environments, which will involve the statistical evaluation of both streamflow discharge and associated physical, chemical, and biological transport phenomena.

Author contributions All authors wrote the main manuscript text. HY and HT developed the model. HY and YY analyzed the data. HY and YY prepared Figures. All authors reviewed the manuscript.

Data availability Data will become available upon reasonable request to the corresponding author.

Declarations

Conflict of interest The authors have no known Conflict of Interest.

Open Access This article is licensed under a Creative Commons Attribution 4.0 International License, which permits use, sharing, adaptation, distribution and reproduction in any medium or format, as long as you give appropriate credit to the original author(s) and the source, provide a link to the Creative Commons licence, and indicate if changes were made. The images or other third party material in this article are included in the article's Creative Commons licence, unless indicated otherwise in a credit line to the material. If material is not included in the article's Creative Commons licence and your intended use is not permitted by statutory regulation or exceeds the permitted use, you will need to obtain permission directly from the copyright holder. To view a copy of this licence, visit http://creativecommons.org/licenses/by/4.0/.

References

Ahmadi-Javid A (2012) Entropic value-at-risk: a new coherent risk measure. J Optim Theor Appl 155:1105–1123. https://doi.org/10.1007/s10957-011-9968-2

Ahmadi-Javid A, Pichler A (2017) An analytical study of norms and Banach spaces induced by the entropic value-at-risk. Math Financ Econ 11(4):527–550. https://doi.org/10.1007/s11579-017-0197-9

Archdeacon TP, Gonzales EJ, Thomas LI (2022) Movement of Red Shiner during a regulated, intentional surface-flow recession. Ecol Freshw Fish 31(2):358–368. https://doi.org/10.1111/eff.12635

Asselman N, de Jong JS, Kroekenstoel D, Folkertsma S (2022) The importance of peak attenuation for flood risk management, exemplified on the Meuse River, the Netherlands. Water Secur 15:100–114. https://doi.org/10.1016/j.wasec.2022.100114

Ávila L, Mine MR, Kaviski E, Detzel DH (2021) Evaluation of hydro-wind complementarity in the medium-term planning of electrical power systems by joint simulation of periodic streamflow and wind speed time series: a Brazilian case study. Renew Energ 167:685–699. https://doi.org/10.1016/j.renene.2020.11.141

Bahrami E, Salarijazi M, Mohammadrezapour O, Haghighat Jou P (2022) Evaluation of SCS model for flood characteristic prediction in an ungauged catchment considering effects of excess rainfall and base flow separation. J Earth Syst Sci 131(1):11. https://doi.org/10.1007/s12040-021-01756-2

Baker SA et al. (2022) The Colorado River Basin operational prediction testbed: a framework for evaluating streamflow forecasts and reservoir operations. JAWRA 58(5):690–708. https://doi.org/10.1111/1752-1688.13038

Barndorff-Nielsen OE (2001) Superposition of Ornstein–Uhlenbeck type processes. Theor Probab Appl 45(2):175–194. https://doi.org/10.1137/S0040585X97978166

Barndorff-Nielsen OE, Stelzer R (2013) The multivariate supOU stochastic volatility model. Math Financ 23(2):275–296. https://doi.org/10.1111/j.1467-9965.2011.00494.x

Bellini F, Laeven RJ, Rosazza Gianin E (2018) Robust return risk measures. Math Financ Econ 12:5–32. https://doi.org/10.1007/s11579-017-0188-x

Bellini F, Laeven RJ, Gianin ER (2021) Dynamic robust Orlicz premia and Haezendonck–Goovaerts risk measures. Eur J Oper Res 291(2):438–446. https://doi.org/10.1016/j.ejor.2019.08.049

Ben-Tal A, Teboulle M (2007) An old–new concept of convex risk measures: the optimized certainty equivalent. Math Financ 17(3):449–476. https://doi.org/10.1111/j.1467-9965.2007.00311.x

Botter G, Porporato A, Rodriguez-Iturbe I, Rinaldo A (2009) Nonlinear storage-discharge relations and catchment streamflow regimes. Water Resour Res 45:10. https://doi.org/10.1029/2008WR007658

Botter G, Basso S, Rodriguez-Iturbe I, Rinaldo A (2013) Resilience of river flow regimes. PNAS 110(32):12925–12930. https://doi.org/10.1073/pnas.1311920110

Canna G, Centrone F, Gianin ER (2021) Haezendonck–Goovaerts capital allocation rules. Insur Math Econ 101:173–185. https://doi.org/10.1016/j.insmatheco.2021.07.004

Catalàn N et al. (2022) Pulse, shunt and storage: hydrological contraction shapes processing and export of particulate organic matter in river networks. Ecosystems 26:873–892. https://doi.org/10.1007/s10021-022-00802-4

Cheridito P, Li T (2008) Dual characterization of properties of risk measures on Orlicz hearts. Math Financ Econ 2:29–55. https://doi.org/10.1007/s11579-008-0013-7

Cheridito P, Li T (2009) Risk measures on Orlicz hearts. Math Finance 19(2):189–214. https://doi.org/10.1111/j.1467-9965.2009.00364.x

Cuchiero C, Teichmann J (2020) Generalized Feller processes and Markovian lifts of stochastic Volterra processes: the affine case. J Evol Equat 20(4):1301–1348. https://doi.org/10.1007/s00028-020-00557-2

Daly E, Calabrese S, Yin J, Porporato A (2019) Linking parametric and water-balance models of the Budyko and Turc spaces. Adv Water Res 134:103435. https://doi.org/10.1016/j.advwatres.2019.103435

Desormeaux C et al. (2022) Investigation of stochastic-threshold incision models across a climatic and morphological gradient. Earth Surface Dyn 10(3):473–492. https://doi.org/10.5194/esurf-10-473-2022

Dowd K, Cotter J, Sorwar G (2008) Spectral risk measures: properties and limitations. J Financ Serv Res 34:61–75. https://doi.org/10.1007/s10693-008-0035-6

Dralle DN et al. (2018) Quantification of the seasonal hillslope water storage that does not drive streamflow. Hydrol Process 32(13):1978–1992. https://doi.org/10.1002/hyp.11627

Ferrazzi M, Botter G (2019) Contrasting signatures of distinct human water uses in regulated flow regimes. Environ Res Commun 1(7):071003. https://doi.org/10.1088/2515-7620/ab3324

Föllmer H, Knispel T (2013) Convex risk measures: Basic facts, law-invariance and beyond, asymptotics for large portfolios. In: MacLean LC William T, Ziemba WT (eds) Handbook of the fundamentals of financial decision making: Part II. World Scientific, Singapore, pp 507–554

Föllmer H, Schied A (2016) Stochastic finance, 4th edn. De Gruyter, Berlin, pp 506–526

Frittelli M, Gianin ER (2004) Dynamic convex risk measures. In: Szegö G (ed) Risk measures for the 21st century. Wiley, New York, pp 227–248

Garbin S, Celegon EA, Fanton P, Botter G (2019) Hydrological controls on river network connectivity. R Soc Open Sci 6(2):181428. https://doi.org/10.1098/rsos.181428

Gómez F, Tang Q, Tong Z (2022) The gradient allocation principle based on the higher moment risk measure. J Bank Financ 143:106544. https://doi.org/10.1016/j.jbankfin.2022.106544

Guo S, Xu H (2022) Robust spectral risk optimization when the subjective risk aversion is ambiguous: a moment-type approach. Math Program 194(1–2):305–340. https://doi.org/10.1007/s10107-021-01630-5

Guo A, Chang J, Wang Y, Wu B, Li Y (2022) Tracing design flood hydrograph uncertainty in reservoir flood control system. Appl Math Model 102:371–384. https://doi.org/10.1016/j.apm.2021.09.012

Hamilton AL, Zeff HB, Characklis GW, Reed PM (2022) Resilient California water portfolios require infrastructure investment partnerships that are viable for all partners. Earth's Future 10(4):e2021EF002573. https://doi.org/10.1029/2021EF002573

Hottovy S, Stechmann SN (2023) Rain process models and convergence to point processes. Nonlin Process Geophys 30(1):85–100. https://doi.org/10.5194/npg-30-85-2023

Kong D, Liu L, Wu Y (2018) Optimal reinsurance under risk and uncertainty on Orlicz hearts. Insur Math Econ 81:108–116. https://doi.org/10.1016/j.insmatheco.2017.10.006

Kouri DP (2019) Spectral risk measures: the risk quadrangle and optimal approximation. Math Program 174(1–2):525–552. https://doi.org/10.1007/s10107-018-1267-3

Lague D (2014) The stream power river incision model: evidence, theory and beyond. Earth Surf Process Landf 39(1):38–61. https://doi.org/10.1002/esp.3462

Li H, Ameli A (2022) A statistical approach for identifying factors governing streamflow recession behaviour. Hydrol Process 36(10):14718. https://doi.org/10.1002/hyp.14718

Li X et al. (2022) Hysteresis analysis reveals dissolved carbon concentration–discharge relationships during and between storm events. Water Res 226:119220. https://doi.org/10.1016/j.watres.2022.119220

Li Y, Chen S, Yin J, Yuan X (2023) A stochastic framework for identification and evaluation of flash drought. Hydrol Earth Syst Sci 27:1077–1087. https://doi.org/10.5194/hess-27-1077-2023

Ma H, Tian D (2021) Generalized entropic risk measures and related BSDEs. Stat Probab Lett 174:109110. https://doi.org/10.1016/j.spl.2021.109110

Malone E et al. (2022) High and dry in days gone by: Life-history theory predicts Appalachian mountain stream fish assemblage transformation during historical drought. Ecol Freshw Fish 31(1):29–44. https://doi.org/10.1111/eff.12606

Merz B et al. (2022) Understanding heavy tails of flood peak distributions. Water Resour Res 58(6):e2021WR030506. https://doi.org/10.1029/2021WR030506

Ministry of Land, Infrastructure, Transport and Tourism (2023) Water information system (in Japanese). http://www1.river.go.jp/. Accessed Feb 14 2023

Mudelsee M (2007) Long memory of rivers from spatial aggregation. Water Resour Res 43:1. https://doi.org/10.1029/2006WR005721

Naqi NM, Al-Madhhachi AST, Al-Jiboori MH (2022) Quantifying Diyala River basin rainfall-runoff models for normal and extreme weather events. Water Pract Technol 17(8):1553–1569. https://doi.org/10.2166/wpt.2022.089

Noto F, Maruyama T, Hayase Y, Takimoto H, Nakamura K (2013) Evaluation of water resources by snow storage using water balance and tank model method in the Tedori River basin of Japan. Paddy Water Environ 11:113–121. https://doi.org/10.1007/s10333-011-0297-8

Philipsen LJ, Rood SB (2022) Riparian recruitment persists after damming: environmental flows and coupled colonization of cottonwoods and willows following floods along a dryland river. River Res Appl 38(9):1642–1653. https://doi.org/10.1002/rra.4030

Rao MM, Ren ZD (2002) Applications of Orlicz spaces. Dekker, New York

Rubshtein BZA, Grabarnik GY, Muratov MA, Pashkova YS (2016) Part IV Orlicz spaces: in foundations of symmetric spaces of measurable functions: Lorentz, Marcinkiewicz and Orlicz spaces. Springer, Cham, pp 171–182

Shabestanipour G et al. (2023) Stochastic watershed model ensembles for long—range planning: verification and validation. Water Resour Res. https://doi.org/10.1029/2022WR032201

Singh VP, Sivakumar B, Cui H (2017) Tsallis entropy theory for modeling in water engineering: a review. Entropy 19(12):641. https://doi.org/10.3390/e19120641

Suyari H, Tsukada M (2005) Law of error in Tsallis statistics. IEEE Trans Inform Theor 51(2):753–757. https://doi.org/10.1109/TIT.2004.840862

Tanaka HA et al. (2015) Optimal synchronization of oscillatory chemical reactions with complex pulse, square, and smooth waveforms signals maximizes Tsallis entropy. Europhys Lett 111(5):50007. https://doi.org/10.1209/0295-5075/111/50007

Tian D (2023) Pricing principle via tsallis relative entropy in incomplete markets. SIAM J Financ Math 14(1):250–278. https://doi.org/10.1137/22M1471614

Tsallis C (2009) Introduction to nonextensive statistical mechanics: approaching a complex world. Springer, New York

Wang Y, Chapman MP (2022) Risk-averse autonomous systems: a brief history and recent developments from the perspective of optimal control. Artif Intell 66:103743. https://doi.org/10.1016/j.artint.2022.103743

Wei C, Fauß M, Chapman MP (2022) CVaR-based safety analysis in the infinite time horizon setting. In: 2022 American control conference (ACC). IEEE, pp 2863–2870. https://doi.org/10.23919/ACC53348.2022.9867285

Wing OE et al. (2020) Toward global stochastic river flood modeling. Water Resour Res 56(8):e2020WR027692. https://doi.org/10.1029/2020WR027692

Yoshioka H (2022) Fitting a superposition of Ornstein–Uhlenbeck process to time series of discharge in a perennial river environment. ANZIAM J 63:C84–C96. https://doi.org/10.21914/anziamj.v63.16985

Yoshioka H, Yoshioka Y (2023) Statistical evaluation of a long-memory process using the generalized entropic value-at-risk. arXiv preprint arXiv:2301.12435

Yoshioka Y et al. (2020) Multiple-indicator study of the response of groundwater recharge sources to highly turbid river water after a landslide in the Tedori River alluvial fan. Jpn Hydrol Process 34(16):3539–3554. https://doi.org/10.1002/hyp.13796

Yoshioka H, Tanaka T, Yoshioka Y, Hashiguchi A (2022) Statistical computation of a superposition of infinitely many Ornstein–Uhlenbeck processes. In: 20th International conference of numerical analysis and applied mathematics (ICNAAM2022), September 19–25, 2022, Sheraton Hotel, Rhodes, Greece and Online (Oral presentation), 4pp article will appear in the proceedings

Yoshioka H, Tanaka T, Yoshioka Y, Hashiguchi A (2023) Stochastic optimization of a mixed moving average process for controlling non-Markovian streamflow environments. Appl Math Model 116:490–509. https://doi.org/10.1016/j.apm.2022.11.009

Yuhi M (2008) Impact of anthropogenic modifications of a river basin on neighboring coasts: case study. J Waterw Port Coast Ocean Eng 134(6):336–344. https://doi.org/10.1061/(ASCE)0733-950X(2008)134:6(336)

Zajkowski K (2020) On norms in some class of exponential type Orlicz spaces of random variables. Positivity 24(5):1231–1240. https://doi.org/10.1007/s11117-019-00729-6

Zimmert J, Seldin Y (2021) Tsallis-inf: an optimal algorithm for stochastic and adversarial bandits. J Mach Learn Res 22(1):1310–1358

Zou Z, Xia Z, Hu T (2022) Tsallis value-at-risk: generalized entropic value-at-risk. Probab Eng Inf Sci. https://doi.org/10.1017/S0269964822000444

Zou Z, Wu Q, Xia Z, Hu T (2023) Adjusted Rényi entropic value-at-risk. Eur J Oper Res 306(1):255–268. https://doi.org/10.1016/j.ejor.2022.08.028